Int. J. Electrochem. Sci., 16 **(2021)** Article Number: 21126, doi: 10.20964/2021.12.06

International Journal of
ELECTROCHEMICAL
SCIENCE
www.electrochemsci.org

Influence of Cl^- and SO_2 on Carbon Steel Q235, Pipeline Steel L415 and Pressure Vessel Steel 16MnNi Corrosion Behavior in Industrial and Marine Atmosphere Environment

Xiaohan Li[1,2], *Gongwang Cao*[2], *Mingxiao Guo*[1,2], *Can Peng*[1,2], *Yunchao Peng*[4], *Kaijun Ma*[4], *Zhenyao Wang*[2,3*]

[1] School of Materials Science and Engineering, University of Science and Technology of China, Shenyang, 110016, China
[2] Institute of Metal Research, Chinese Academy of Sciences, Shenyang, 110016, China
[3] Liaoning Shenyang Soil and Atmosphere Corrosion of Material National Observation and Research Station, Shenyang, 110016, China
[4] PipeChina network corporation eastern oil storage and transportation Co. Ltd.
Author information
[*]E-mail: zhywang@imr.ac.cn

Received: 8 June 2021 / *Accepted:* 5 July 2021 / *Published:* 10 November 2021

Zhanjiang is a typical industrial Marine atmosphere environment and there are large amounts of Cl^- and SO_2 contained in atmosphere. These two constituents contribute to the corrosion of carbon steel Q235, pipeline steel L415, pressure vessel steel 16MnNi at the Zhanjiang oil station. In this study, a wet-dry cyclic accelerated experiment was carried out to study the difference in corrosion behavior of three type of steels under Cl^- and SO_2. The results indicated that the empirical formula $D = At^n$ was suitable for corrosion kinetics of three materials. At the same exposure time and under the same corrosion conditions, the corrosion degree of three materials was: carbon steel Q235 > pipeline steel L415 > pressure vessel steel 16MnNi. There were the same corrosion products of three materials, and the corrosion degree was determined by the relative content of α-FeOOH and γ-FeOOH. Additional, Cl^- was found to play a decisive role in the corrosion rate.

Keywords: Atmospheric corrosion; Zhanjiang; Q235 carbon steel; L415 pipeline steel; 16MnNi pressure vessel steel.

1. INTRODUCTION

Zhanjiang has a superior geographical location, facing the sea, and with convenient transport, so the oil station was built near the coast. Carbon steel (CS) Q235 could work as the material for the oil tank pressure ring. Pipeline steel (PS) L415 is used for oil and gas transportation. Pressure vessel steel

(PVS) 16MnNi is widely used as the outer wall material of an oil storage tank owing to its good compressive properties. The Zhanjiang oil station approaches to the coast and has higher Cl^- in the atmosphere than inland. In addition, there is also a certain concentration of SO_2 due to the burning of fossil fuels. Cl^- has a strong hygroscopic ability, and thus, it is easy to wet the sample surface and form a liquid film on the metal surface. Moreover, Cl^- has better permeability, which can destroy the protection of the rust layer and react directly with the substrate. Thus, Cl^- accelerates corrosion. Additional, SO_2 is easily soluble in water and oxidized to H_2SO_4, which can react with the substrate or rust layer. During the reaction process, the corrosion product $FeSO_4$ regenerates H_2SO_4, and the reaction could continue forever[1, 2]. These corrosive factors seriously affects the service life of common materials at Zhanjiang oil station, resulting in perforation and leakage, which could bring serious losses to the national economy and ecological environment. However, there is little research that the corrosion behavior of common materials used in oil stations under the Cl^- and SO_2. Mao et al. [3] researched the influence of Cl^- in $NaHCO_3$ solution on the corrosion resistance and passivation of pipeline steels and found that corrosion pits in $NaHCO_3$ solution containing Cl^- were larger than those without Cl^- . Li et al. [4] reported that by continuous monitored solution resistance and polarization resistance, Cl^- and SO_2 could accelerate the corrosion rate of Q235 (CS).

The corrosion behavior of the metal materials can be investigated using outdoor exposure test [5-7] and indoor laboratory accelerated test [8-10]. Through the outdoor exposure test, the real and reliable information on the corrosion of the metals can be obtained, but the process requires a longer time than indoor laboratory accelerated experiment. Also, there are many uncontrollable variables compared with indoor experiment, resulting in poor data repeatability. Therefore, many researchers take the indoor laboratory accelerated test to research the corrosion process of steel. It is common knowledge that the steel exposures to atmospheric environment will occur an electrochemical process between the metal surface and surrounding environment [11-13]. Due to the cycle of nights and days, the temperature and humidity vary periodically, which changes the thickness of the aqueous film regularly. The concentration of the corrosive solution increases during the drying process, and increasing the frequency of wet-dry alternation will accelerate the corrosion rate [6]. Therefore, the wet-dry alternation accelerated test is a better method among different indoor simulation accelerated methods.

In this study, NaCl and Na_2SO_4 were used as the corrosive medium, and the influence of Zhanjiang typical corrosion factors Cl^- and SO_2 on the corrosion behavior of Q235 (CS) L415 (PS) and 16MnNi (PVS) was simulated by indoor wet-dry cycle tests. The corrosion samples were mainly studied by weight loss analysis, corrosion product analysis, corrosion morphology observation, and electrochemical analysis to research the difference in corrosion behavior of the three steels under the same environment.

2. EXPERIMENT

2.1 Experimental materials

For this research, three types of experimental materials were prepared, namely Q235 (CS), L415 (PS) and 16MnNi (PVS), which are composed as follows (Table 1). Because of different analysis

experiment requirements, two sizes of samples need to be prepared. Four parallel samples were cut into the dimensions of 50mm × 25mm × 5mm. Before using the four samples, there were ultrasonically cleaned in acetone, then cleaned in alcohol and distilled water. After drying for 24h, the samples were weighed (with a precision of 0.1 mg) and stored. The other size was 10mm × 10mm × 5mm for the electrochemical measurements (three parallel samples), connected with wires, and sealed with epoxy resin, these samples were mechanically polished to 2000 grit by using the different SiC paper, then cleaned with distilled water, finally, dried for 24h. Based on the average concentration of Cl^- and SO_2 in the Zhanjiang atmosphere, the 0.2mol/L NaCl + 0.05mol/L Na_2SO_4 was used as the corrosive solution.

Table 1. Major composition of three materials (mass%).

Materials	Major composition							
	C	Si	P	S	Cr	Mn	Fe	Ni
16MnNi(PVS)	0.11	0.26	0.011	<0.003	0.03	1.32	rest	0.03
L415(PS)	0.08	0.16	0.015	<0.003	/	1.61	rest	/
Q235(CS)	0.15	0.11	0.033	0.010	0.05	0.36	rest	0.03

2.2 Experimental methods

The C4-180 apparatus can simulate the process of wet-dry cycle to perform the indoor accelerated test. A cycle procedure was as follows: 90%RH for 2h and then 60%RH for 2h, and a constant temperature of 35 ℃. Before the experiment, the corrosive solution of 20μL/cm^2 was uniformly deposited on the sample, which was then placed in an oven to dry, finally, all samples were put into the climatic test chamber, every 48h, this step was repeated. After 48h, 96h, 192h, 336h, 528h, the corrosion samples were analyzed separately.

2.3 Weight loss

The rust layer on the sample surface was removed for the composition analysis. According to the GB/T16545-2015, the rest of the corrosion products were placed in a solution that contained 500 mL (38 wt%) hydrochloric acid + 500 mL distilled water + 3.5 g hexamethylenetetramine at 23℃. The samples were gently cleaned with a brush until there were no products on the substrate, and then quickly cleaned in distilled water and alcohol, dried, stored in a desiccator at least 24h. Finally, the mass of the samples was determined by using an electronic balance.

2.4 Characterization of corrosion products

The phase compositions of the corrosion products were analyzed using X-ray diffraction (XRD). The XRD was carried out by using Cu K_α target under 50kV and 250mA at the range of 10°-70°, with a scan speed was 10°/min. By using the amount of powder in each XRD samples to test was the same, the

differences of the intensity for the different XRD samples can be compared. Therefore, the intensity of each phase of the corrosion products can semi-quantitatively reflects its relative content [2].

The element contents and element distribution of the rust layer were analyzed using an energy dispersive spectrometer (EDS). The macro-morphology on the surface of samples was recorded by digital camera. The scanning electron microscopy (SEM) was used to observe the surface micro-morphologies and cross-sectional morphologies of the corroded samples.

2.5 Electrochemical measurements

The Electrochemical Impedance Spectroscopy (EIS) and potentiodynamic polarization measurement could react greatly the electrochemical characteristic of metal materials. The PARSTAT 2273 with a classical three-electrode system was used to perform the electrochemical measurements, the electrolyte was 0.1mol/L Na_2SO_4 aqueous solution. Corroded samples, saturated calomel electrode and clean platinum plate served as the working electrode, reference electrode and counter electrode, respectively. The scan rate was 0.33mV/s, the scan range was from -250mV (SCE) relative to the open circuit potential (OCP) to 0V (SCE). The amplitude of the AC voltage was 10mV and the frequency range was 10^5Hz ~ 10^{-2}Hz. When the OCP is stabilized, the EIS and potentiodynamic polarization measurement can be executed.

3. RESULT AND DISCUSSION

3.1 Weight mass loss experiments

Although the weight loss could directly and clearly reflect the corrosion situation of the metal materials, in general, the thickness loss can better evaluate the corrosion behavior of the samples, the calculation formula of the thickness loss is as follow [5, 14]:

$$D = \frac{10000(w_o - w_s)}{\rho S} \quad (1)$$

where D is the loss of thickness (μm), w_o is the weight before the test (g), w_s is the weight after the test (g), ρ is the density (7.86g·cm^{-3}) and S is the working area of the samples (cm^2). The relative relationship between the thickness loss and time of the three materials can be expressed through the power empirical formula [15-17]:

$$D = At^n \quad (2)$$

where D is the loss of thickness (μm), t is the corrosion time (h), A and n are constants. The value of n represents the protection of the rust layer: if $n > 1$, it means that corrosion products has poor protection to substrate and facilitates the corrosion process; if $n < 1$, the corrosion products can protect the matrix well and inhibit the corrosion process; if $n = 1$, the corrosion rate is a stable value [18]. Figure 1 (a) shows the fitting lines of thickness loss and time, it can be seen that $R^2 > 0.99$ and $n > 1$ of the three materials, the corrosion process of the three materials was an accelerated process. From the thickness loss, when Q235 (CS), L415 (PS) and 16MnNi (PVS) worked at the same environment, the corrosion

resistance of L415 (PS) and 16MnNi (PVS) was better than that of Q235 (CS).To further research the corrosion process of the three materials, the corrosion rate of the samples at different corrosion time was obtained by the following equation [19, 20] :

$$V_D = \frac{D_n - D_{n-1}}{t_n - t_{n-1}} \quad (3)$$

where V_D is the corrosion rate (μm/h), D_n is the thickness loss(μm), t is the corrosion time (h), and n is the period of samples (n = 1, 2, 3, 4, 5 correspond to samples corrosion for 48, 96, 192, 336, 528h, respectively). Figure 1 (b) presents the corrosion rate of Q235 (CS), L415 (PS) and 16MnNi (PVS) at different times. The corrosion rate of the three materials had the same changing trend with time, which increased at early time and decreased subsequently. The dense rust layer protected the matrix in the later period and inhibited the corrosion process, which decreased the corrosion rate of the three materials after 336h. Q235 (CS) had the highest corrosion rate throughout the experiment, and the corrosion rate of L415 (PS) was higher than that of 16Mn (PVS), so the degree of corrosion degree for the three materials was: Q235 (CS) > L415 (PS) > 16MnNi (PVS). However, the content of manganese in Q235 (CS) was lower than that in L415 (PS) and 16MnNi (PVS), which was different from the earlier conclusions that increasing the content of manganese accelerates the corrosion process [21, 22]. Therefore, the corrosion process of L415 (PS) and 16MnNi (PVS) under the Cl^- and SO_2 need to be further researched.

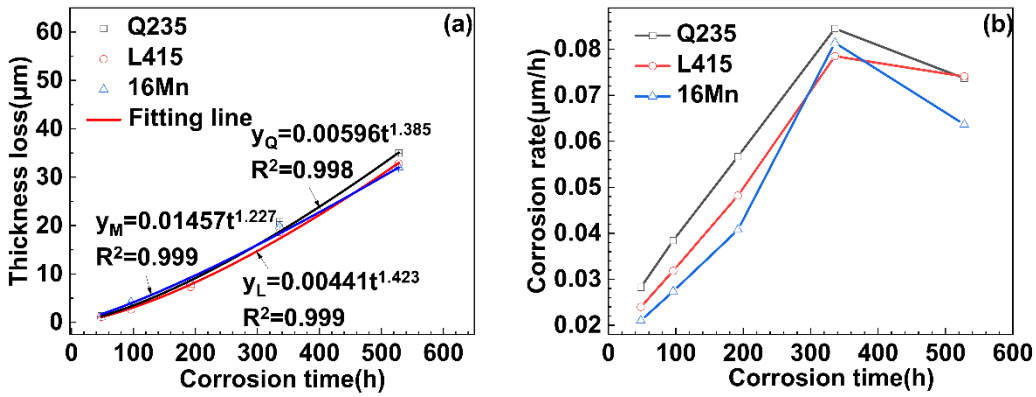

Figure 1. (a)Variation of thickness loss of Q235 (CS), L415 (PS) and 16MnNi (PVS) with time, (b) Variation of corrosion rate of Q235 (CS), L415 (PS) and 16MnNi (PVS) with time.

3.2 Morphology of rust layer

Figure 2 shows the macro-morphology of the rust layer of Q235 (CS), L415 (PS) and 16MnNi (PVS) at different times. As can be seen from the figure, the color of the rust layer of the three materials changed with time. The color of the rust layer formed on Q235 (CS) was orange at first, then gradually changed to yellow-orange, and finally the surface of rust layer was reddish-brown. At the beginning of the experiment, the surface of the samples was covered by a great number of spots. The area of these spots gradually increased and spots clumped together to form a local complete rust layer. 16MnNi (PVS) had the same color transition behavior and formation process of rust layer as the Q235 (CS). However,

the initial color of the L415 (PS) rust layer was originally yellow, which may be caused by the presence of more α-FeOOH in the early experiment, because the color of α-FeOOH is yellowish brown [23]. After that, the L415 (PS) had the same color transition behavior as Q235 (CS) and also formed a partial and complete rust layer.

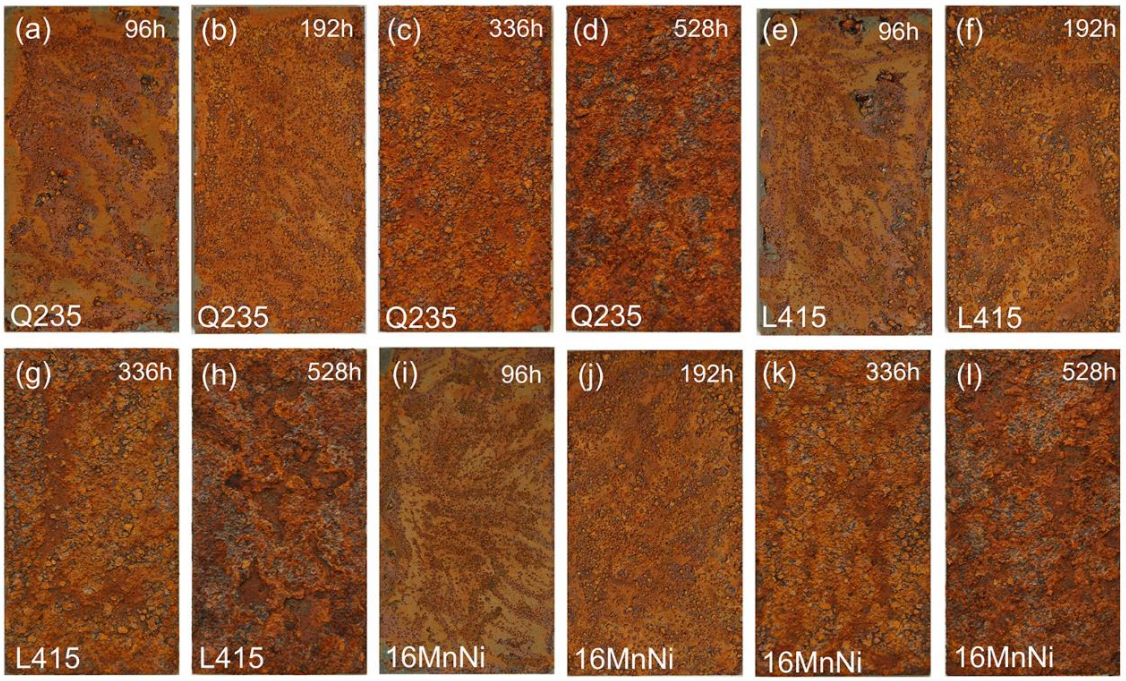

Figure 2. Macro-morphology of the rust layer of Q235 (CS), L415 (PS) and 16MnNi (PVS) after 96h, 192h, 336h, 528h.

Figure 3 shows the micro-morphology of the rust layer of Q235 (CS), L415 (PS) and 16MnNi (PVS) at 48h, 192h and 528h. The surface of Q235 (CS), L415 (PS) and 16MnNi (PVS) formed humps at first, and there were some micro-cracks on the humps. With time passed by, the corrosion products were uniformly distributed on the substrate. At 192h, the radius of the holes in the Q235 (CS) rust layer was larger than other materials. Although the surface roughness of Q235 (CS) decreased at 528h, it was still higher than that of L415 (PS) and 16MnNi (PVS). The rough surface and larger pores were conductive to promoting the penetration of the corrosive solution, which caused the weight loss of Q235 (CS) was higher than that of L415 (PS) and 16MnNi (PVS).

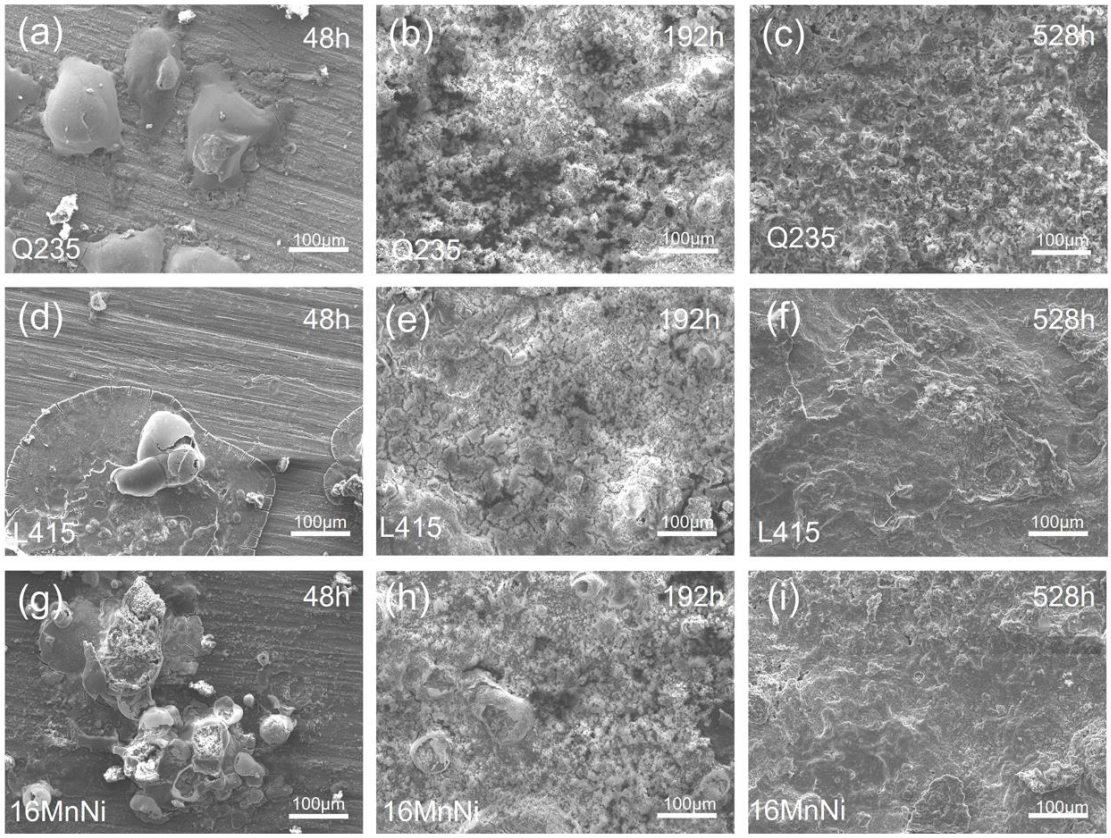

Figure 3. Micro-morphology of rust layer of Q235 (CS), L415 (PS) and 16MnNi (PVS) at 48h, 192h and 528h.

The structure of the rust layer directly affects the corrosion behavior of the steel. As shown in Figure 4, a compact rust layer was formed on the matrix of the three materials with time passed by. At 528h, compared with the rust layer of Q235 (CS), the rust layer of 16MnNi (PVS) had a higher density, while the L415 (PS) had a compact inner rust layer.

Figure 5 shows the distribution of corrosion factors of the three materials at different times, the distribution of sulfur in the rust layer was relatively uniform, and the distribution of chlorine transformed from uniform to unevenly throughout the experiment. To further demonstrate the influence of Cl^- and SO_2 on the corrosion process of the three materials. Table 2 shows the content of chlorine and sulfur at the points marked in Figure 4. The content of chlorine reduced first and then increased with time. At the beginning of the experiment, although the rust layer thickened with time, the rust layer had numerous holes and was loosely bound to the substrate. Therefore, the rust layer easily fell off from the substrate, which reduced the thickness of the rust layer and caused the content of chlorine to decrease. Later, a compact rust layer was gradually formed to have a better protective effect on the substrate, but Cl^- has the better permeability and could easily pass through the rust layer to the matrix, so the content of Cl^- increased with time.

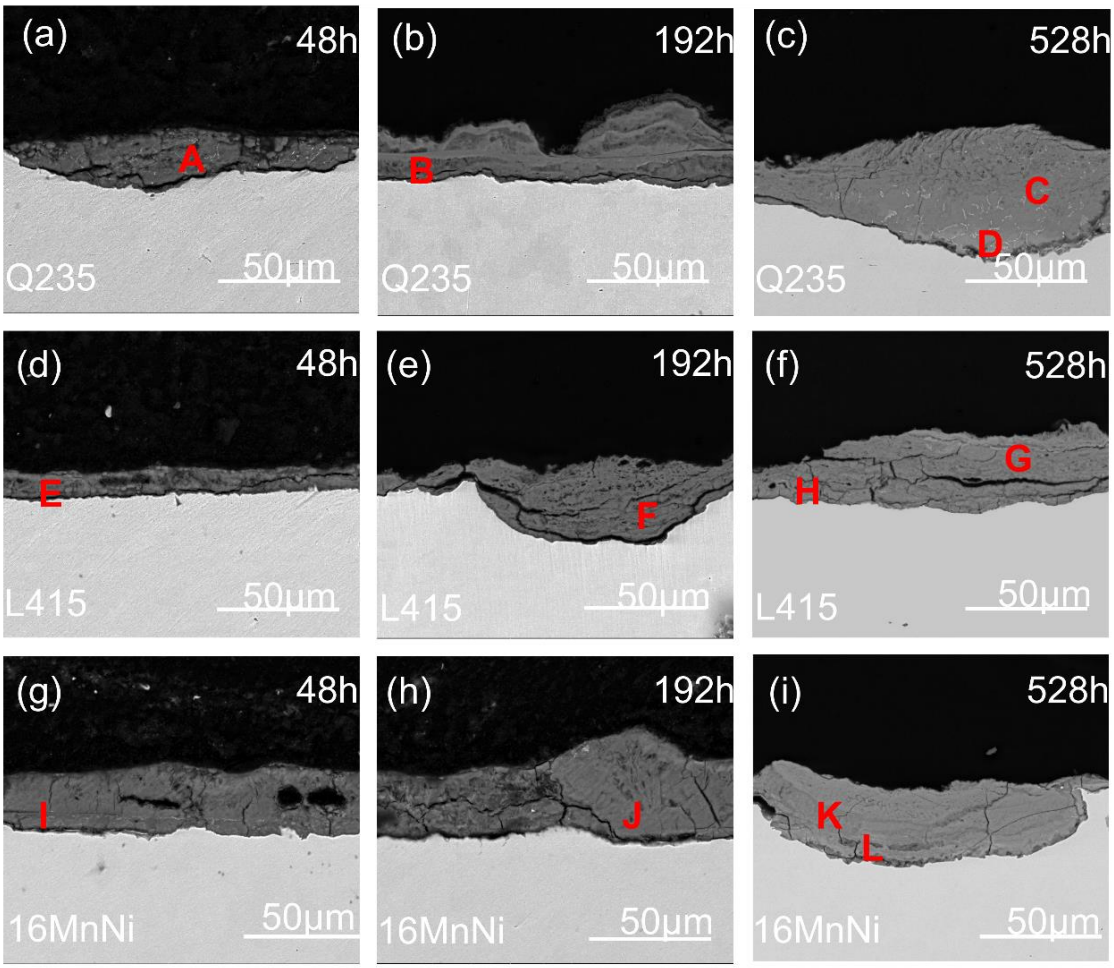

Figure 4. Cross-sectional morphology of Q235 (CS), L415 (PS) and 16MnNi (PVS) after 48h, 192h, 528h.

The existence of Cl^- is the prerequisite for the formation of β-FeOOH, and the β-FeOOH can be partially converted to γ-FeOOH. Both corrosion products can accelerate the corrosion process. Table 2 indicates the content of Cl^- in the rust layer of Q235 (CS) was always higher than that of L415 (PS) and 16MnNi (PVS), which caused the number of β-FeOOH and γ-FeOOH of Q235 (CS) was always higher than that in other materials, so the Q235 (CS) had the highest corrosion rate. However, the content of sulfur little changed during the experiment. It shows that Cl^- is the major factor affecting the corrosion process rather than SO_2.

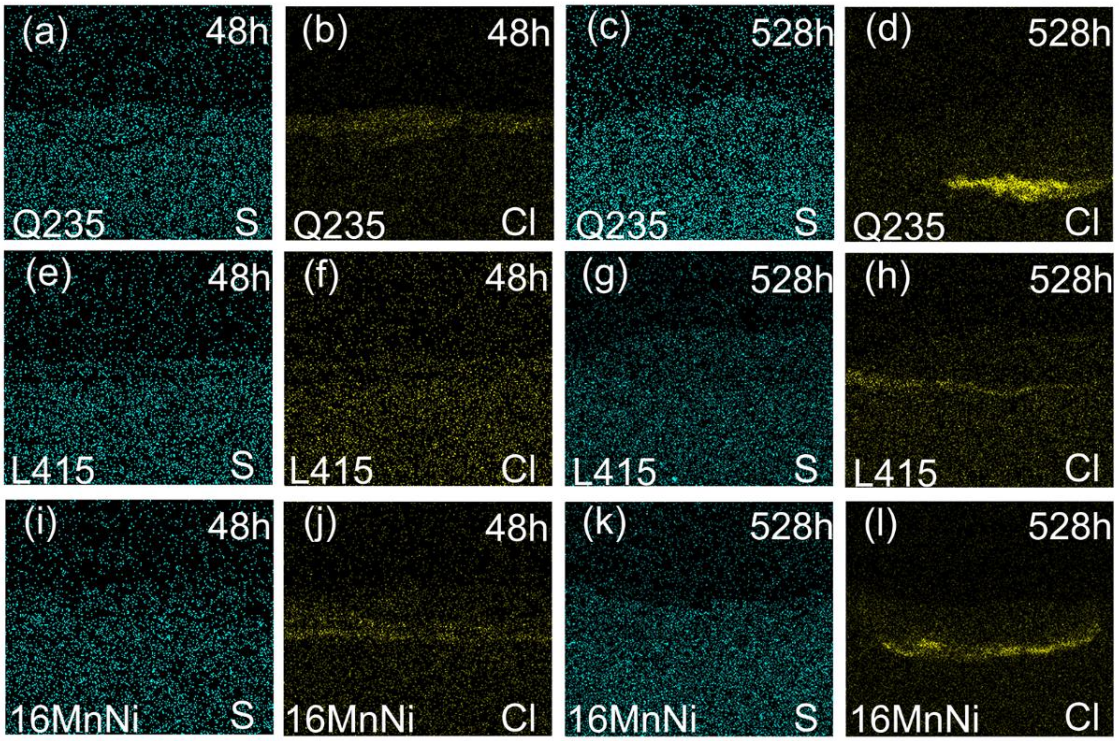

Figure 5. The element distribution of S and Cl of Q235 (CS), L415 (PS) and 16MnNi (PVS) at 48h and 528h.

Table 2. The content of anions at the point marked in Figure 4 (wt%).

	A	B	C	D	E	F
O	52.63	62.66	61.94	53.85	53.89	62.42
S	/	0.45	0.16	0.53	0.01	/
Cl	3.87	0.36	0.9	10.34	2.54	0.21
Fe	43.5	36.53	37	35.28	43.56	36.8

	G	H	I	J	K	L
O	62.12	50.85	60.78	59.8	61.91	57.23
S	0.14	0.42	0.93	0.03	0.07	0.02
Cl	0.39	2.44	1.01	0.21	0.99	5.31
Fe	37.35	46.3	37.28	39.95	37.04	37.44

3.3 Composition of corrosion product

The composition of the rust layer can influence the variation of corrosion rate, therefore, the corrosion process can be explained by studying the corrosion products. In generally, the rust layer of steel mainly contains α-FeOOH, Fe_2O_3, β-FeOOH, Fe_3O_4, γ-FeOOH and amorphous substances [24-26].

Figure 6 (a) shows the XRD pattern of the Q235 (CS) rusty powder at different times. There was plenty of α-FeOOH, γ-FeOOH, and a small amount of β-FeOOH, Fe_2O_3 and Fe_3O_4 in the rust layer.

Among them, β-FeOOH appeared at the beginning of the experiment and the peak strength of the β-FeOOH decreased with time. The diffraction peak intensity of γ-FeOOH initially increased then remained stable throughout the experiment. Fe_3O_4 was close to the substrate and could not be easily detected. Therefore, the diffraction peak intensity of Fe_3O_4 was lower than that of other products. In the early phase of the experiment, the intensity of α-FeOOH increased significantly with time, and then remained basically unchanged in the later phase of the experiment. Figure 6 (b) and Figure 6 (c) express the XRD results of the rust layer formed on L415 (PS) and 16MnNi (PVS) with time, respectively. It shows that L415 (PS) and 16MnNi (PVS) had the same products as Q235 (CS), but the peak strength of γ-FeOOH in L415 (PS) reduced slightly at 528h, while the peak strength of γ-FeOOH in 16MnNi (PVS) decreased significantly.

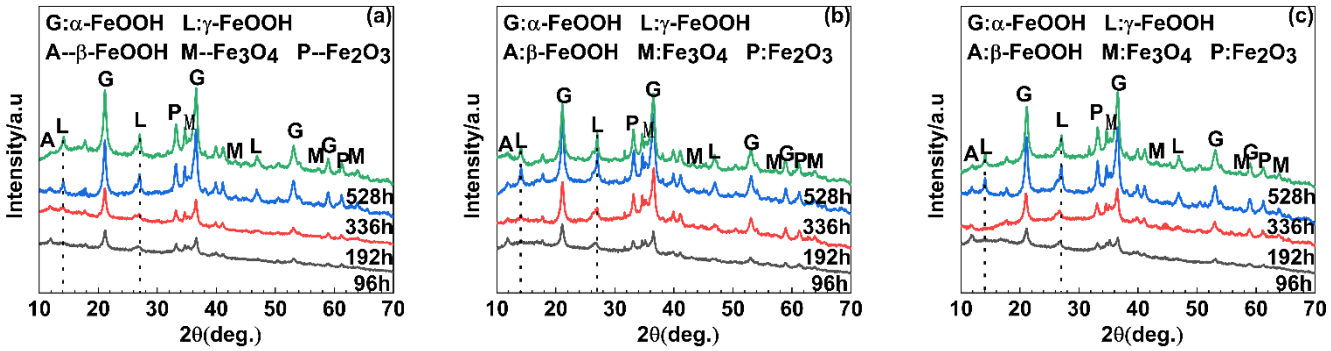

Figure 6. XRD pattern of powdered rust formed on Q235 (CS), L415 (PS) and 16MnNi (PVS) at the 96h, 192h, 336h, 528h: (a) Q235 (CS), (b) L415 (PS) and (C) 16MnNi (PVS).

A comparison of the XRD pattern of three materials showed that the corrosion products were the same in the same environment, but the peak intensity of corrosion products was different. In addition, there were no manganese compounds detected in the corrosion products of L415 (PS) and 16MnNi (PVS), although there was more manganese in the matrix of L415 (PS) and 16MnNi (PVS). It indicates that manganese existed stably in this environment and had no effect on the corrosion process.

The oxidation order of the corrosion products is: β-FeOOH > γ-FeOOH > α-FeOOH [27]. Some researchers have found that the presence of Cl^- promotes the formation of β-FeOOH, which is highly reducible and beneficial to the corrosion process [5, 28, 29]. During the experiment, the iron dissolved in the solution containing Cl^-, generated $FeCl_2$ and transformed to green rust, finally, the β-FeOOH was formed on the substrate. Because β-FeOOH is easily converted to other corrosion products, the intensity of β-FeOOH decreased in the later stage of the experiment. The phase of γ-FeOOH was the major oxidant and participated in the cathodic reaction, thus expediting the corrosion process. γ-FeOOH can be converted to chemically stable α-FeOOH and Fe_3O_4 [30]. α-FeOOH is a relatively stable product that can inhibit the anodic reaction and decreases the corrosion rate [31, 32]. The formation of α-FeOOH is favorable in the Na_2SO_4 solution film, it demonstrates that SO_4^{2-} promotes the formation of α-FeOOH

[26], so α-FeOOH can be observed in the corrosion products of three materials at 48h. Additionally, the content of α-FeOOH increased continuously due to the transformation from γ-FeOOH and Fe_3O_4 [33, 34]:

$$8\gamma\text{-FeOOH} + Fe^{2+} + 2e^- \rightarrow 3Fe_3O_4 + 4H_2O \quad (4)$$

$$Fe_3O_4 + 1/4O_2 + 3/2H_20 \rightarrow 3\alpha\text{-FeOOH} \quad (5)$$

3.4 Electrochemical measurements

The atmospheric corrosion of metals is an electrochemical process under thin electrolyte film [35], therefore, the potentiodynamic polarization measurement and EIS were used to analyze the properties of the rust layer under different materials at different times. The potentiodynamic polarization curves of Q235 (CS), L415 (PS) and 16MnNi (PVS) in 0.1mol/L Na_2SO_4 solution are shown in Figure 7. The evolutionary process of the polarization curves of the three kinds of materials was similar, indicating that the corrosion mechanism was the same. At the beginning of the experiment, oxygen gas was dissolved in the aqueous film of the rust layer surface, and the reduction of oxygen was the primary cathodic reaction while the anodic process was controlled by the dissolution reaction of iron [6, 36]:

$$\text{Anodic: } Fe + 2e^- \rightarrow Fe^{2+} \quad (6)$$

$$\text{Cathodic: } O_2 + H_2O + 4e^- \rightarrow 4OH^- \quad (7)$$

As the time went on, the cathodic current increased gradually and then tended to be stable at the later stage of the experiment, while the anodic current gradually decreased. It indicates that the reduction of the rust layer was the main cathodic reaction rather than the reduction of oxygen, and the anodic reaction was inhibited. The decreased of the anodic current due to the continuous transformation of γ-FeOOH to the stable α-FeOOH.

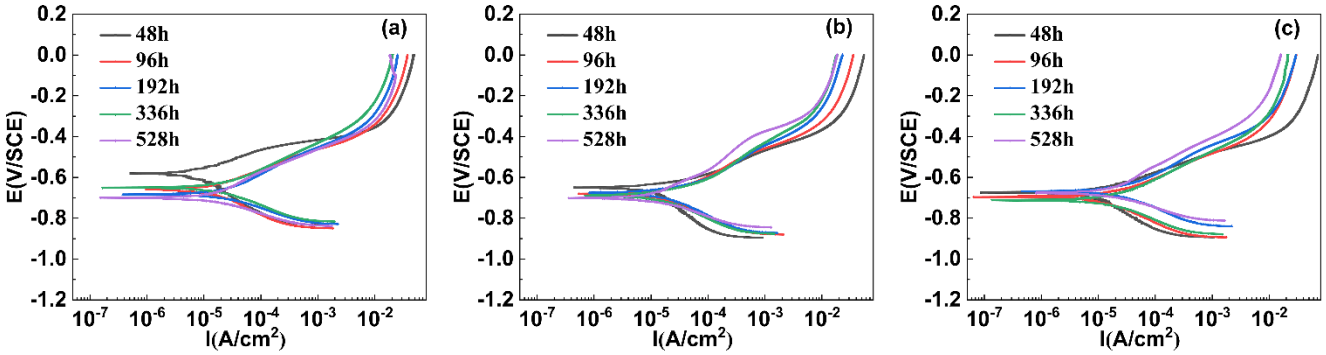

Figure 7. Potentiodynamic polarization curves of Q235 (CS), L415 (PS) and 16MnNi (PVS) were immersed in 0.1mol/L Na_2SO_4 electrolyte: (a) Q235 (CS), (b) L415 (PS) and (C) 16MnNi (PVS).

The corrosion potential (E_{corr}) and corrosion current density (I_{corr}) can be calculated by Tafel extrapolation, as shown in Table 3, the I_{corr} increased initially and subsequently decreased. From the beginning of the experiment to 336h, the I_{corr} of Q235 (CS), L415 (PS) and 16MnNi (PVS) increased

continuously, but the I_{corr} decreased after 336h. Moreover, the I_{corr} order of the three materials was: Q235 (CS) > L415 (PS) > 16MnNi (PVS). The corrosion current density is positively correlated with the corrosion rate, so the order of corrosion rate was Q235 (CS) > L415 (PS) > 16MnNi (PVS). The result of current density is in agreement with the corrosion rate with time in Figure 1 (b).

Table 3. Corrosion potential (E_{corr}) and corrosion current density (I_{corr}) of Q235 (CS), L415 (PS) and 16MnNi (PVS) fitted from the polarization curve by Tafel extrapolation.

Experiment time /h	Q235 (CS)		L415 (PS)		16MnNi(PVS)	
	E_{corr} /mV	I_{corr} /μA·cm^{-2}	E_{corr} /mV	I_{corr} /μA·cm^{-2}	E_{corr} /mV	I_{corr} /μA·cm^{-2}
48	-655	4.49	-649	13.52	-689	7.47
96	-658	22.50	-716	16.14	-693	15.67
192	-693	28.96	-680	18.24	-668	17.43
336	-674	33.05	-705	22.51	-668	29.28
528	-669	16.80	-730	13.47	-682	12.08

Table 4. Charge transfer resistance of Q235 (CS), L415 (PS) and 16MnNi (PVS) rusted layer at different immersion time

Immersion time/h	Q235 (CS)	L415 (PS)	16MnNi(PVS)
	Rct(Ω·cm^2)	Rct(Ω·cm^2)	Rct(Ω·cm^2)
48	750.2	832.7	843.5
96	633.3	634.1	639.8
192	552.1	508.7	578.2
336	500.2	588.3	557.8
528	933.5	958.4	698.3

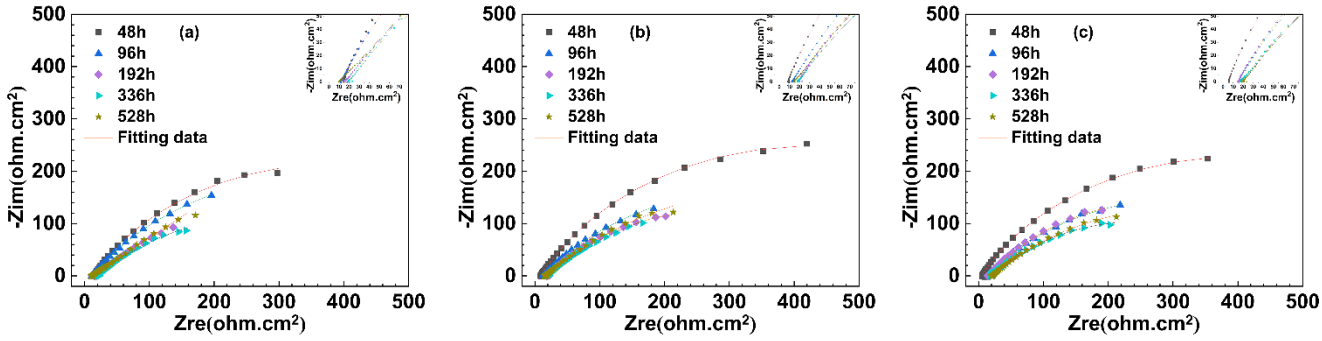

Figure 8. Nyquist diagrams of Q235 (CS), L415 (PS) and 16MnNi (PVS) in 0.1mol/L Na_2SO_4 electrolyte: (a) Q235 (CS), (b) L415 (PS) and (c) 16MnNi (PVS).

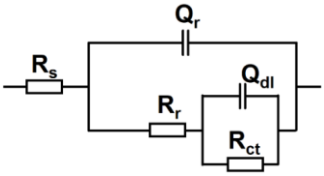

Figure 9. Equivalent circuit of Q235 (CS), L415 (PS) and 16MnNi (PVS).

Figure 8 shows the Nyquist diagrams of Q235 (CS), L415 (PS) and 16MnNi (PVS) at different times. Figure 9 is the equivalent circuit used for the EIS data. In Figure 9, R_s represents the solution resistance, R_r represents the rust layer resistance, R_{ct} represents the charge transfer resistance, Q_r and Q_{dl} represent the rust layer capacitance and double-layer capacity, respectively. However, Q235 (CS) and 16MnNi (PVS) had no two-layered structure in the rust layer at 528h, because the inner rust layer gradually changed into the outer rust layer over time. Consequently, it is also required to consider the two layers as a whole. Generally, R_{ct} can better reflect the corrosion resistance of materials[37, 38] than R_p. Table 4 shows that the trend of R_{ct} of the three materials decreased first and then increased with time, indicating that the compact rust layer and stable corrosion products inhibited the corrosion process of the three materials in the later.

4. CONCLUSION

The corrosion behavior of Q235 (CS), L415 (PS) and 16MnNi (PVS) under Cl^- and SO_2 at Zhanjiang oil station was researched, the following results were obtained:

(1) The corrosion kinetics of Q235 (CS), L415 (PS) and 16MnNi (PVS) conformed to the empirical equation: $D = At^n$ and the value of n was greater than 1 of three materials.

(2) Three materials were exposed to the same corrosive environment, Q235 (CS) had the least corrosion resistance, while 16MnNi (PVS) had the best corrosion resistance.

(3) Three materials formed the same corrosion products under the same environment that contained lots of α-FeOOH and γ-FeOOH, a little β-FeOOH, $Fe_3O_4$and Fe_2O_3.

(4) The influence of Cl^- on the corrosion process was greater than that of SO_4^{2-}.

(5) Q235 (CS), L415 (PS) and 16MnNi (PVS) formed a dense rust layer at the later stage of the experiment, which inhibited the corrosion process and decreased the corrosion rate.

ACKNOWLEDGEMENT
The investigation is supported by PipeChina network corporation eastern oil storage and transportation Co.,Ltd, Liaoning Shenyang Soil and Atmosphere Corrosion of Material National Observation and Research Station.

References

1. L. Hao, S. Zhang, J. Dong and W. Ke, *Metall. Mater. Trans. A.*, 43 (2011) 1724.
2. W. Chen, L. Hao, J. Dong and W. Ke, *Corros. Sci.*, 83 (2014) 155.

3. X. Mao, X. Liu and R.W. Revie, *Corrosion*, 50 (1994) 651.
4. X. Li, X. Wang, L. Wang, Y. Sun, B. Zhang, H. Li, Y. Huang and B. Hou *J. Mater. Eng. Perform.*, 28 (2019) 2327.
5. Y. Ma, Y. Li and F. Wang, *Corros. Sci.*, 51 (2009) 997.
6. W. Han, C. Pan, Z. Wang and G. Yu, *Corros. Sci.*, 88 (2014) 89.
7. D. de la Fuente, I. Díaz, J. Simancas, B. Chico and M. Morcillo, *Corros. Sci.*, 53 (2011) 604.
8. J. Yu, H. Wang, Y. Yu, Z. Luo, W. Liu and C. Wang, *Corros. Sci.*, 133 (2018) 276.
9. C. Thee, L. Hao, J. Dong, X. Mu, X. Wei, X. Li and W. Ke, *Corros. Sci.*, 78 (2014) 130.
10. X. Lu, Y. Liu, M. Liu and Z. Wang, *J. Mater. Sci. Technol. (Shenyang, China)*, 35 (2019) 1831.
11. X. Fu, J. Dong, E. Han and W. Ke, *Sensors (Basel)*, 9 (2009) 10400.
12. W. Han, G. Yu, Z. Wang and J. Wang, *Corros. Sci.*, 49 (2007) 2920.
13. Y. Cai, Y. Zhao, X. Ma, K. Zhou and Y. Chen, *Corros. Sci.*, 137 (2018) 163.
14. Y. Ma, Y. Li and F. Wang, *Corros. Sci.*, 52 (2010) 1796.
15. Q. Yu, C.-f. Dong, Y.-h. Fang, K. Xiao, C.-y. Guo, G. He and X.-g. Li, *J. Iron Steel Res. Int.*, 23 (2016) 1061.
16. T.T.N. Lan, N.T.P. Thoa, R. Nishimura, Y. Tsujino, M. Yokoi and Y. Maeda, *Corros. Sci.*, 48 (2006) 179.
17. F. Iwei, *Br. Corros. J.*, 26 (2013) 209.
18. Y. Liu, *Int. J. Electrochem. Sci.*, 14 (2019) 1147.
19. Y. Liu, *Int. J. Electrochem. Sci.*,15 (2020) 6464.
20. Y. Ma, Y. Li and F. Wang, *Mater. Chem. Phys.*, 112 (2008) 844.
21. S. Fajardo, I. Llorente, J.A. Jiménez, J.M. Bastidas and D.M. Bastidas, *Corros. Sci.*, 154 (2019) 246.
22. G. Su and X. Gao, *Mater.*, 10 (2017) 938.
23. A.A.O$_{\text{LOWE}}$, P$_{\text{H}}$.R$_{\text{EFAIT}}$ and J.M.R.Genin, *Corros. Sci.*, 32 (1991) 1003.
24. K. Asami and M. Kikuchi, *Corros. Sci.*, 45 (2003) 2671.
25. H. Antony, L. Legrand, L. Maréchal, S. Perrin, P. Dillmann and A. Chaussé, *Electrochim. Acta.*, 51 (2005) 745.
26. M. Yamashita, H. Konishi, T. Kozakura, J. Mizuki and H. Uchida, *Corros. Sci.*, 47 (2005) 2492.
27. H. Antony, S. Perrin, P. Dillmann, L. Legrand and A. Chaussé, *Electrochim. Acta*, 52 (2007) 7754.
28. N.S. Palsson, K. Wongpinkaew, P. Khamsuk, S. Sorachot and W. Pongsaksawad, *Mater. Corros.*, 71 (2019) 1019.
29. C. Pan, W. Han, Z. Wang, C. Wang and G. Yu, *J. Mater. Eng. Perform.* 25 (2016) 5382.
30. Y.Y. Chen, H.J. Tzeng, L.I. Wei, L.H. Wang, J.C. Oung and H.C. Shih, *Corros. Sci.*, 47 (2005) 1001.
31. L. Hao, S. Zhang, J. Dong and W. Ke, *Corros. Sci.*, 59 (2012) 270.
32. T. Kamimura, S. Nasu, T. Segi, T. Tazaki, S. Morimoto and H. Miyuki, *Corros. Sci.*, 45 (2003) 1863.
33. L. Song, X. Ma, Z. Chen and B. Hou, *Corros. Sci.*, 87 (2014) 427.
34. C. Pan, M. Guo, W. Han, Z. Wang and C. Wang, *Corros. Eng., Sci. Technol.*, 54 (2019) 241.
35. F. Corvo, J. Minotas, J. Delgado and C. Arroyave, *Corros. Sci.*, 47 (2005) 883.
36. Z. Wang, M. Wang, J. Jiang, X. Lan, F. Wang, Z. Geng and Q. Tian, *Scanning*, 2020 (2020) 9591516.
37. K. Ding, W. Guo, R. Qiu, J. Hou, L. Fan and L. Xu, *J. Mater. Eng. Perform.*, 27 (2018) 4489.
38. M. Guo, *Int. J. Electrochem. Sci.*, 16 (2021) 210457

© 2021 The Authors. Published by ESG (www.electrochemsci.org). This article is an open access article distributed under the terms and conditions of the Creative Commons Attribution license (http://creativecommons.org/licenses/by/4.0/).